

# Deformation mechanisms in a metastable beta titanium twinning induced plasticity alloy with high yield strength and high strain hardening rate

Gao, Junheng; Huang, Yuhe; Guan, Dikai; Knowles, Alexander J.; Ma, Le; Dye, David; Rainforth, W. Mark

DOI:

[10.1016/j.actamat.2018.04.035](https://doi.org/10.1016/j.actamat.2018.04.035)

License:

Creative Commons: Attribution (CC BY)

*Document Version*

Publisher's PDF, also known as Version of record

*Citation for published version (Harvard):*

Gao, J, Huang, Y, Guan, D, Knowles, AJ, Ma, L, Dye, D & Rainforth, WM 2018, 'Deformation mechanisms in a metastable beta titanium twinning induced plasticity alloy with high yield strength and high strain hardening rate', *Acta Materialia*, vol. 152, pp. 301-314. <https://doi.org/10.1016/j.actamat.2018.04.035>

[Link to publication on Research at Birmingham portal](#)

## General rights

Unless a licence is specified above, all rights (including copyright and moral rights) in this document are retained by the authors and/or the copyright holders. The express permission of the copyright holder must be obtained for any use of this material other than for purposes permitted by law.

- Users may freely distribute the URL that is used to identify this publication.
- Users may download and/or print one copy of the publication from the University of Birmingham research portal for the purpose of private study or non-commercial research.
- User may use extracts from the document in line with the concept of 'fair dealing' under the Copyright, Designs and Patents Act 1988 (?)
- Users may not further distribute the material nor use it for the purposes of commercial gain.

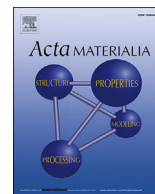
Where a licence is displayed above, please note the terms and conditions of the licence govern your use of this document.

When citing, please reference the published version.

## Take down policy

While the University of Birmingham exercises care and attention in making items available there are rare occasions when an item has been uploaded in error or has been deemed to be commercially or otherwise sensitive.

If you believe that this is the case for this document, please contact [UBIRA@lists.bham.ac.uk](mailto:UBIRA@lists.bham.ac.uk) providing details and we will remove access to the work immediately and investigate.



## Full length article

# Deformation mechanisms in a metastable beta titanium twinning induced plasticity alloy with high yield strength and high strain hardening rate

Junheng Gao<sup>a</sup>, Yuhe Huang<sup>a</sup>, Dikai Guan<sup>a</sup>, Alexander J. Knowles<sup>b</sup>, Le Ma<sup>a</sup>, David Dye<sup>b</sup>, W. Mark Rainforth<sup>a,\*</sup>

<sup>a</sup> Department of Materials Science and Engineering, The University of Sheffield, S1 3JD, UK

<sup>b</sup> Department of Materials, Royal School of Mines, Imperial College, London, SW7 2AZ, UK

## ARTICLE INFO

## Article history:

Received 30 January 2018

Received in revised form

13 April 2018

Accepted 14 April 2018

Available online 17 April 2018

## ABSTRACT

Metastable  $\beta$  titanium alloys with both twinning (TWIP) and martensite transformation (TRIP) usually exhibit a low yield strength of between 200 and 500 MPa, but high strain hardening rate and large uniform elongation. Alloys that exhibit twinning on a single system provide a higher yield strength, but a lower strain hardening rate. Here, for the first time, we report a new alloy (Ti-7Mo-3Cr wt%) with both high yield strength (695 MPa) and high work hardening rate ( $\sim 1900$  MPa) and a substantial 33.3% uniform elongation. The deformation mechanisms were systematically investigated using EBSD and TEM for samples strained to 1.3%, 5% and 16%. The high yield strength was achieved through initial deformation mechanisms of two twin systems, namely both  $\{332\}\langle 113 \rangle$  and  $\{112\}\langle 111 \rangle$  twinning. Importantly, the martensite transformation was suppressed at this stage of deformation. The combination of two twin systems, with approximately the same intensity, resulted in a high strain hardening rate (1600 MPa  $\sim 1900$  MPa), much greater compared to alloys that exhibit a single twin system. Moreover, the TRIP effect was observed at strains greater than 5%, which also contributed to the high strain hardening rate large uniform elongation.

© 2018 Acta Materialia Inc. Published by Elsevier Ltd. This is an open access article under the CC BY license (<http://creativecommons.org/licenses/by/4.0/>).

## 1. Introduction

Metastable  $\beta$  titanium alloys are potentially attractive for applications including biomedical and containment due to their combination of high strength, ductility, density around  $4.5 \text{ g/cm}^3$ , high corrosion resistance, low elastic modulus and low biotoxicity [1–12]. Recently, considerable effort has been devoted to developing new metastable  $\beta$  titanium alloys due to their ability to exhibit large uniform elongation and high strain hardening rate. It has been reported that with an increase in the  $\beta$  phase chemical stability, the deformation mechanisms of metastable  $\beta$  titanium alloys change from martensite transformation, to mechanical twinning and eventually, dislocation slip [12,13]. The chemical stability of the  $\beta$  phase is believed to be connected to the values of two electronic parameters, Bo (the covalent bond strength between Ti and the alloying elements) and Md (the mean d-orbital energy

level) [8,14,15]. Based on the Bo-Md map originally proposed by Kuroda et al. [15] and later by Abdel-Hady et al. [8,15] for superelastic titanium alloys, several metastable  $\beta$  titanium alloys have been developed (including Ti-12Mo [13] and Ti-9Mo-6W [16] (hereafter all the compositions are in mass%)) with both TRIP and TWIP in the initial deformation stage. These offer a peak strain hardening rate as high as 2000 MPa but a low yield strength generally below 500 MPa. Sun et al. [19] studied the early stage deformation mechanisms of Ti-12Mo alloy, finding that a strain/stress induced phase transformation ( $\beta$  to orthorhombic  $\alpha''$ ) and primary twinning such as  $\{332\}\langle 113 \rangle$  and  $\{112\}\langle 111 \rangle$  were activated simultaneously. They believed that  $\{332\}\langle 113 \rangle$  twinning and subsequent secondary twinning dominated the early stages of the deformation process. Recently, Yao et al. [17] investigated the plastic deformation of Ti-24Nb-4Zr-8Sn and their results showed that the stress-induced  $\beta$  to  $\alpha''$  martensitic transformation occurred first with a yield strength of  $\sim 200$  MPa, giving rise to a stress plateau (pseudoelasticity); subsequently  $\{112\}\langle 111 \rangle$  twinning occurred, resulting in a high strain hardening rate. Sun et al.

\* Corresponding author.

E-mail address: [m.rainforth@sheffield.ac.uk](mailto:m.rainforth@sheffield.ac.uk) (W.M. Rainforth).

reported that low temperature aging at 423 K for 60s can effectively increase the yield strength of the Ti-12Mo alloy from 480 MPa to 730 MPa and avoid the stress plateau observed on the onset of plastic deformation in solid-solution-treated Ti-12Mo alloy [18]. Clearly, the stress-induced martensitic transformation leads to pseudo-elasticity and therefore low yield strength and limited work hardening, as observed in Ti-10V-3Fe-3Al [19] and Ti-Nb alloys [4,20]. In metastable  $\beta$  titanium alloys, the twinning system is often observed to be  $\{332\} \langle 113 \rangle$ , in contrast to the  $\{112\} \langle 111 \rangle$  twinning system observed in more heavily  $\beta$  stabilized alloys [13,21–23].

Metastable  $\beta$  titanium alloys with initial deformation mechanisms of both TRIP and TWIP generally exhibit a low yield strength between 200 and 500 MPa (e.g. Ti-24Nb-4Zr-8Sn (~200 MPa) [17], Ti-12Mo (~480 MPa) [13], Ti-9Mo-6W (480 MPa) [16] and Ti-10V-3Fe-3Al. This is because the critical stress for martensite transformation ranges between 190 MPa and 360 MPa, depending on the strain rate [19]. These alloys exhibit a high strain hardening rate and large uniform elongation. The second class of metastable  $\beta$  titanium alloys, that have been of considerable interest in the last few years, only exhibit twinning and dislocation slip (e.g. Ti-10Cr [24], Ti-15Mo [25] and Ti-10Mo-1Fe [26]). These specific deformation mechanisms, i.e., twinning and dislocation slip, result in a relatively higher yield strength, but a low straining hardening rate. In this case the  $\{332\} \langle 113 \rangle$  is usually the only dominant the twin system that is activated.

In this work, an alloy was designed to specifically deform by twinning, but on two twin systems, to provide a high yield strength. The alloy design had to displace the formation of martensite to higher stresses, which when combined with the twin evolution on two systems would lead to both high yield strength and high work hardening. Cr was selected as one alloy addition on the basis that Ti-Cr alloys exhibit the TWIP effect leading to high yield strength, large elongation and good corrosion resistance [24,27]. The composition was adjusted to yield values of Bo of 2.80 and Md of 2.40, respectively. According to the Bo-Md map provided by Abdel-Hady et al. [8,15], the position of Ti-7Mo-3Cr alloy (Ti-73) is at the boundary between twinning and dislocation glide, which is a relatively unexplored region of the Bo-Md map. Our hypothesis was that this region would avoid the formation of martensite during the initial deformation and would provide both dislocation glide and twinning. Moreover, we believed that this region would provide twinning on both  $\{332\} \langle 113 \rangle$  and  $\{112\} \langle 111 \rangle$  systems.

The mechanical properties of this newly proposed Ti-73 alloy were studied in tension and the deformation mechanisms were systematically studied by EBSD and TEM. Quantitative evaluation of the strain hardening effect of  $\{112\} \langle 111 \rangle$  and  $\{332\} \langle 113 \rangle$  twinning was conducted. Several new deformed microstructures, such as the formation of high density parallel  $\{112\} \langle 111 \rangle$  twins and the interaction of two sets of high density parallel  $\{112\} \langle 111 \rangle$  twin variants were investigated. Thus, by careful selection of chemical composition, we successfully designed a new alloy with a high yield strength of 710 MPa, high strain hardening rate of ~1900 MPa and 32% uniform elongation, which successfully addressed the drawback of low yield strength of  $\beta$  titanium alloy with both TRIP and/or TWIP effects and poor strain hardening of TWIP metastable  $\beta$  titanium alloys.

## 2. Experimental

The Ti-7Mo-3Cr alloy was prepared from pure elements by arc melting in a low pressure, high-purity argon atmosphere. An ingot was then cast into a  $6 \times 7 \times 30$  mm water cooled copper mould. The ingot was then homogenized at 1200°C for 3 h under flowing argon and water quenched. It was then cold rolled from 6 to 2.4 mm

thickness, annealed at 850°C for 20 min under flowing argon, and water quenched. The Ti, Mo and Cr contents were analysed using an inductively coupled plasma method (ICP-OES instrument) and the O concentration was determined by an inert gas fusion-infrared absorption method (Leco ONH836 instrument). The nominal and analysed chemical compositions are listed in Table 1. The shear modulus (G) of annealed Ti-73 alloy was determined using ultrasonic method (OLYMPUS EPOCH 650). Shear modulus can be expressed as  $G = \rho V_s^2$  [28], where  $V_s$  is the ultrasonic shear wave velocity and  $\rho$  is the density of the material. The bulk density of the Ti-73 alloy was determined by the Archimedes method using a balance (New Classic MF MS104S/01) with an accuracy of  $\pm 0.0001$  g. Tensile samples with  $3 \times 12.5 \times 2.4$  mm gauge section were cut and polished from the annealed plate. Tensile tests were then performed along the rolling direction (RD) using a laser extensometer at a nominal strain rate of  $4 \times 10^{-4} \text{ s}^{-1}$ . Three samples were tested to failure, with another three interrupted tests performed to total strains of 1.3%, 5% and 16%, for electron backscatter diffraction (EBSD) and transmission electron microscopy (TEM) analysis. These strain levels were selected based on the hardening behaviour: just after yield, at the minimum strain hardening rate of ~1600 MPa, and at the maximum strain hardening rate observed of ~1900 MPa. Samples for backscatter electron (BSE) and EBSD imaging were mechanically polished down to 3  $\mu\text{m}$  diamond suspension and twin-jet electropolished with a solution of 5% perchloric acid, 35% 2-butoxyethanol and 60% methanol. In order to obtain a high quality region for EBSD mapping at magnification of  $500\times$ , the samples were electropolished for a short time (30–40 s) to remove the residual deformation in the surface layer induced by mechanical polishing. Prior to EBSD observation, the samples were polished using a Gatan Precision Ion Polishing (PIP-SII) system at 0.5 kV,  $2^\circ$  for 0.5 h. In order to be able to locate the rolling/loading direction, EBSD samples were cut from gauge section with one straight edge. BSE imaging and EBSD were performed using a field emission gun scanning electron microscope (FEI Inspect F50 FEG SEM) operating at 10 kV for BSE imaging and 20 kV for EBSD with a step size of 1  $\mu\text{m}$  for grain size analysis and 0.15  $\mu\text{m}$  for twinning and phase analysis. EBSD data were analysed using HKL's CHANNEL5 software. After EBSD, the thin foils from the tensile tests were cleaned in acetone and twin-jet electropolished again to get electron transparent region in the sample solutions for TEM analysis. A Tecnai T20 transmission electron microscope operated at 200 kV was used to characterize the annealed and deformed samples.

To determine the grain size effect on the activation of  $\{332\} \langle 113 \rangle$  twinning and twin system selection in an individual grain, the Schmid factor (SF) of the 12 variants for both  $\{332\} \langle 113 \rangle$  and  $\{112\} \langle 111 \rangle$  twinning systems were calculated and the variants possessing an absolute value of SF higher than 0.3 are given in Tables 2 and 3 and Supplementary Table 1. In order to make the SF analysis more statistically significant, more than 20 grains in total were analysed. The SF is defined similarly to slip using  $\text{SF} = \cos \phi \cos \lambda$ , where  $\phi$  and  $\lambda$  are the angles between the tensile direction and the twinning direction and the normal to the twinning plane, respectively. The tensile direction was marked on the sample prior to analysis, allowing the straight forward calculation of the angles. The values of  $\phi$  and  $\lambda$  are taken between  $0^\circ$  and  $180^\circ$ , so the SF values ranged between  $-0.5$  and  $0.5$ . The orientation

**Table 1**  
Nominal and analysed chemical compositions of Ti-73 alloy in wt.%.

Elements	Ti	Mo	Cr	O
Nominal composition	Bal.	7	3	0
Analysed composition	Bal.	6.73	2.92	0.12

**Table 2**

Twin variants of  $\{332\}\langle 113 \rangle$  twinning system for which  $|SF| > 0.3$  in grains 1, 2 and 3 in Fig. 4b.

Grain 1		Grain 2		Grain 3	
$\{332\}\langle 113 \rangle$	SF	$\{332\}\langle 113 \rangle$	SF	$\{332\}\langle 113 \rangle$	SF
$(332)[11\bar{3}]$	<b>0.444</b>	$(233)[\bar{3}11]$	0.318	$(332)[11\bar{3}]$	<b>0.457</b>
$(323)[1\bar{3}1]$	0.382	$(3\bar{3}2)[1\bar{1}\bar{3}]$	<b>0.488</b>	$(2\bar{3}3)[\bar{3}11]$	<b>0.457</b>
$(233)[\bar{3}11]$	0.330	$(323)[1\bar{3}1]$	−0.359	$(32\bar{3})[1\bar{3}1]$	−0.377
$(32\bar{3})[1\bar{3}1]$	−0.444				

index of tensile direction in each analysed grain was determined using HKL's CHANNEL5 software, which was used to calculate the values of  $\cos \varphi$  and  $\cos \lambda$ . The twinning variants with positive SF tend to activate in tension, while with negative SF tend to activate in compression. It was assumed that no twin variants would be activated where the SF was lower than 0.3 [12].

### 3. Results

#### 3.1. Microstructural analysis of the Ti-73 alloy annealed at 850°C for 20 min

After annealing at 850°C for 20 min, the Ti-73 alloy exhibited a broad grain size distribution, with maximum observed grain size of 190  $\mu\text{m}$  and a minimum grain size of 12  $\mu\text{m}$ , Fig. 1. The EBSD map indicated a single phase microstructure free from annealing twins and second phases.

TEM analysis identified the presence of hexagonal  $\omega$  phase in

the  $\beta$ , Fig. 2, as previously observed in water quenched metastable  $\beta$  titanium alloys [29–31]. Selected area diffraction using the  $[113]_{\beta}$  zone axis confirmed the expected  $[\bar{1}13]_{\beta}/[1\bar{2}13]_{\omega_1}$  orientation relationship. Fig. 2c provides a corresponding dark field image, showing the distribution of  $\omega_1$  in the  $\beta$ .

#### 3.2. Mechanical behaviour in the annealed condition

Fig. 3a shows a typical uniaxial tensile engineering stress-strain curve of the Ti-73 alloy annealed at 850°C for 20 min. The figure includes the full tensile curve when tested to failure and the interrupted curves, which exhibited excellent reproducibility. The yield strength, ultimate tensile strength and uniform elongation were measured to be 695 MPa, 909 MPa and 33.3% from the engineering stress-strain curve. Fig. 3b shows the true stress-strain curve and the corresponding strain-hardening rate curve. After yielding, the annealed Ti-73 alloy exhibited pronounced strain hardening up to the peak strength of 1260 MPa. After yielding, the strain hardening rate dropped continuously to 1600 MPa at a strain of 4.9%. From 4.9% to 10% true strain, the work hardening rate stabilized at around 1600 MPa. Beyond 10% true strain, the strain hardening rate increased monotonically to a maximum value of 1900 MPa at 17.3% strain, followed by a steady decrease to 32% strain, at which point necking began. According to Considère's criterion, the uniform elongation was 32%.

#### 3.3. Microstructural analysis after 1.3% total strain

The sample deformed to 1.3% total strain ( $\sim 0.2\%$  plastic strain) is

**Table 3**

Twinning variants of both  $\{332\}\langle 113 \rangle$  and  $\{112\}\langle 111 \rangle$  twinning systems for which  $|SF| > 0.3$  in grains 1, 2, 4 and 5 in Fig. 6b.

Grain 1		Grain 2		Grain 4		Grain 5	
$\{112\}\langle 111 \rangle$	SF	$\{112\}\langle 111 \rangle$	SF	$\{112\}\langle 111 \rangle$	SF	$\{112\}\langle 111 \rangle$	SF
$(21\bar{1})[1\bar{1}1]$	−0.401	$(21\bar{1})[1\bar{1}1]$	−0.303	$(21\bar{1})[1\bar{1}1]$	0.399	$(21\bar{1})[1\bar{1}1]$	<b>0.409</b>
		$(21\bar{1})[11\bar{1}]$	−0.471	$(12\bar{1})[\bar{1}11]$	−0.32	$(1\bar{1}2)[\bar{1}11]$	−0.451
		$(\bar{1}21)[11\bar{1}]$	<b>0.336</b>	$(2\bar{1}1)[11\bar{1}]$	<b>0.489</b>	$(121)[1\bar{1}\bar{1}]$	<b>0.409</b>
		$(121)[\bar{1}1\bar{1}]$	0.302	$(\bar{2}11)[\bar{1}\bar{1}\bar{1}]$	0.398		
				$(\bar{1}21)[11\bar{1}]$	−0.326		
				$(\bar{1}12)[1\bar{1}\bar{1}]$	−0.380		
				$(211)[1\bar{1}\bar{1}]$	<b>0.489</b>		
$\{332\}\langle 113 \rangle$	SF	$\{332\}\langle 113 \rangle$	SF	$\{332\}\langle 113 \rangle$	SF	$\{332\}\langle 113 \rangle$	SF
$(332)[11\bar{3}]$	0.385	$(3\bar{2}3)[131]$	−0.413	$(\bar{2}33)[311]$	−0.443	$(\bar{2}33)[311]$	−0.402
$(2\bar{3}3)[\bar{3}11]$	<b>0.480</b>	$(\bar{3}32)[1\bar{1}\bar{3}]$	0.368	$(23\bar{3})[\bar{3}11]$	−0.448	$(\bar{3}32)[1\bar{1}\bar{3}]$	<b>0.419</b>
$(323)[\bar{1}31]$	0.388	$(23\bar{3})[\bar{3}11]$	<b>0.478</b>			$(323)[1\bar{3}1]$	0.335
		$(32\bar{3})[1\bar{3}1]$	−0.331			$(2\bar{3}3)[\bar{3}11]$	−0.469

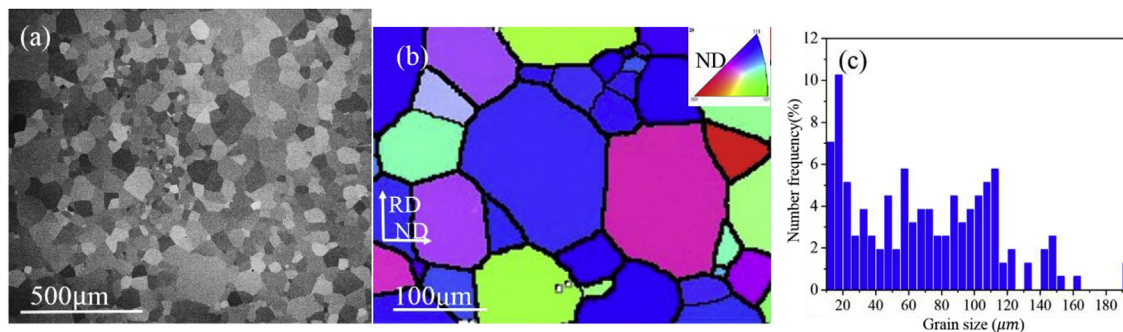


**Fig. 1.** Microstructural analysis of the Ti-73 alloy annealed at 850°C for 20 min. (a) Low magnification BSE image (b) EBSD inverse pole figure (IPF) map of the annealed Ti-73 alloy. (c) Grain size distribution of the annealed alloy, obtained from a low magnification EBSD map containing 260 grains.



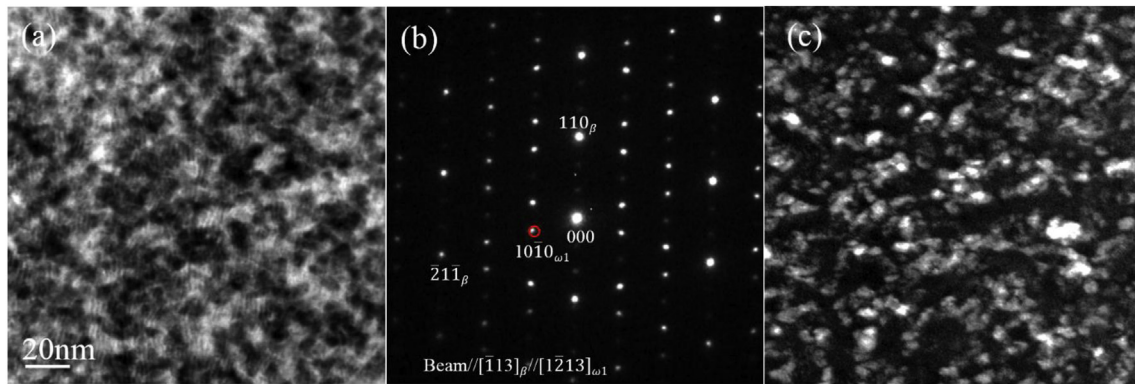


**Fig. 2.** TEM analysis of the Ti-73 alloy annealed at 850°C for 20 min. (a) Bright-field (BF) micrograph. (b) SAED pattern with beam  $// [113]_{\beta} // [1213]_{\omega 1}$ . (c) Dark-field (DF) micrograph recorded using  $(1010)_{\omega 1}$  diffraction spot (circled in selected-area electron diffraction (SAED) pattern in (b)).

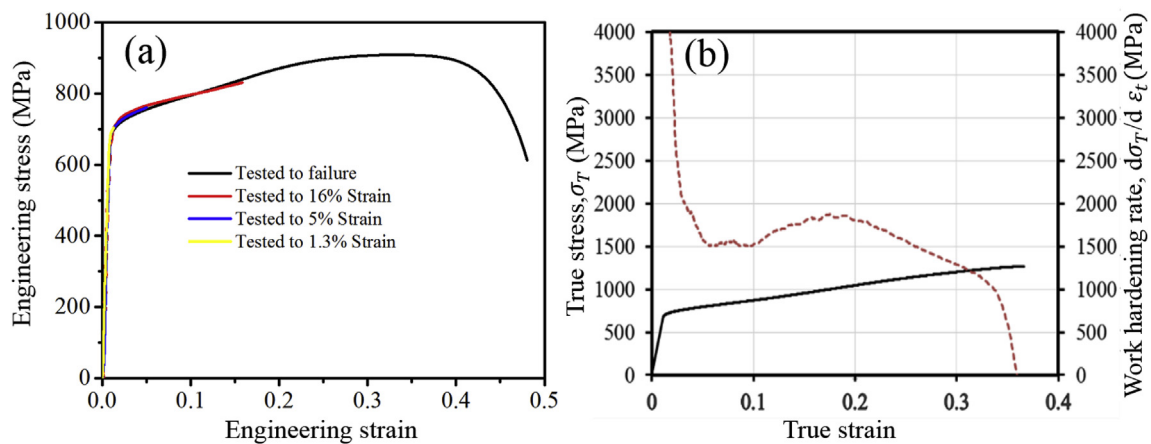


**Fig. 3.** Tensile true stress-strain curves of the Ti-73 alloy annealed at 850°C for 20 min. (a) Engineering stress-strain curves, both tested to failure and interrupted curves are present. (b) True stress-strain curve (black line) and the strain hardening rate,  $d\sigma_T/d\varepsilon_T$  (red dashed line) are present. (For interpretation of the references to colour in this figure legend, the reader is referred to the Web version of this article.)

shown in Fig. 4. One  $\{332\}<113>$  twin was observed in the largest grain; several thin non-indexed deformation bands are also evident. TEM analysis was conducted to investigate these non-indexed deformation bands and whether other deformation mechanisms such as martensite transformation,  $\{112\}<111>$  twinning and the  $\omega$  phase transformation were activated. This

showed that, in addition to the  $\{332\}<113>$  twins observed in Fig. 4, both an isolated  $\{112\}<111>$  twin (Fig. 5a) and high density parallel  $\{112\}<111>$  twins (Fig. 5d) were present. Fig. 5b shows that the isolated  $\{112\}<111>$  twin was  $\sim 480$  nm wide, which is much wider than that the  $\{112\}<111>$  twins in Fig. 5d and e. As shown in Fig. 5e, the DF image recorded using  $(110)_{\beta}$  diffraction spot (red circle in

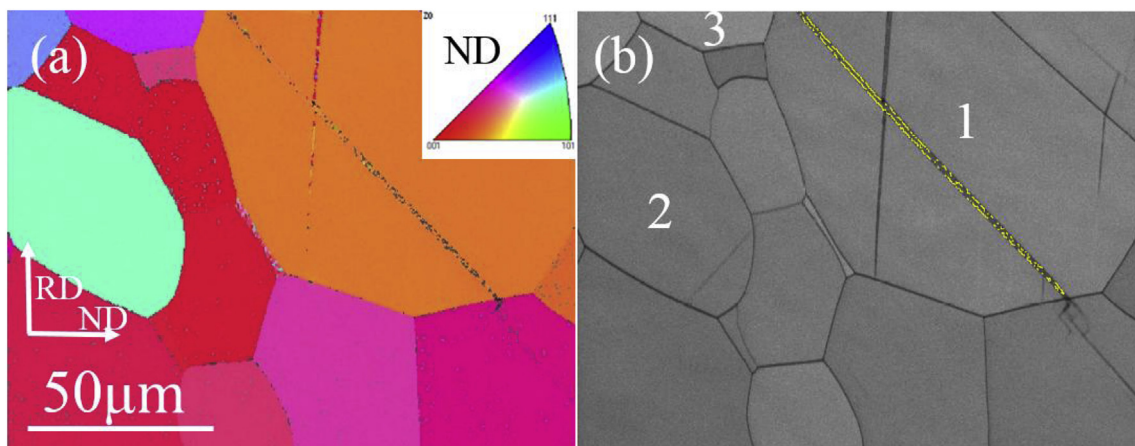


**Fig. 4.** EBSD analysis of the Ti-73 alloy subjected to a strain of 1.3% in tension. (a) IPF map superimposed by band contrast (BC). (b) BC map superimposed with  $\{332\}<113>$  twin boundary (yellow). (For interpretation of the references to colour in this figure legend, the reader is referred to the Web version of this article.)

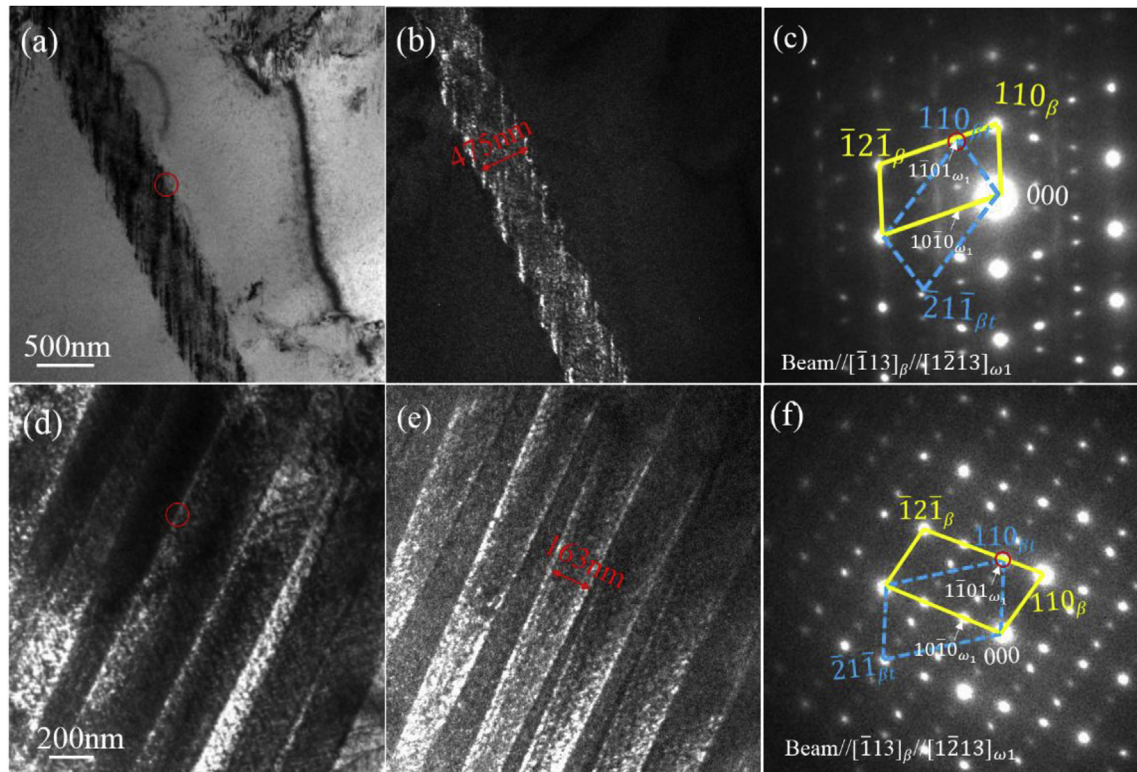


**Fig. 5.** TEM analysis of the tensile sample after 1.3% total strain. (a) BF image and its indexed  $\beta[113]$  zone axis SAED pattern (c) recorded from the red circle marked area in (a). (b) DF image using  $(110)_{\beta t}$  and  $(1\bar{1}01)_{\omega 1}$  diffraction spot, red circle in (c). (d) BF image showing the formation of parallel deformation bands and its indexed  $\beta[113]$  zone axis SAED pattern (f). (e) DF image of  $(110)_{\beta t}$  diffraction spot, red circle in (f). (For interpretation of the references to colour in this figure legend, the reader is referred to the Web version of this article.)

Fig. 5f) shows that these high density parallel  $\{112\}<111>$  twins have a width of  $\sim 160$  nm, interleaved with thinner regions of untwinned matrix, e.g. the bottom-right corner of Fig. 5d. A preferential distribution of  $\omega_1$  at the twin boundaries of both individual and parallel  $\{112\}<111>$  twins was observed in Fig. 5b and e. The preferential distribution of  $\omega$  at  $\{112\}<111>$  twin boundaries was also observed in Ti-Nb alloy [31,32], which Lai et al. proposed that the interfacial formation of  $\omega$  phase during  $\{112\}<111>$  twinning or martensite transformation ( $\alpha''$ ) was attributed to  $\{2\ 1\ 1\}_{\beta}<111>_{\beta}$  shear [31]. Zhang et al. [2] suggested a complexion-mediated transformation to interpret the formation mechanisms of nanolaminate composite microstructure, consisting of adjacent orthorhombic  $\alpha''$ ,  $\omega$  planar complexion and twinned  $\alpha''$  nanolayer. In addition to the twinning, extensive dislocation activity was observed, Supplementary Figure 1, with the  $\{332\}<113>$  twin boundary appearing to act as a barrier to slip. No martensite transformation was observed at this strain.

#### 3.4. Microstructural analysis after deformation to 5% strain

An overview of the sample deformed to 5% strain is provided in Fig. 6. Individual grains 1–5 are labelled in Fig. 6b. In grains 1–3, only  $\{332\}<113>$  twins were observed. In grains 1–3, the  $\{112\}<111>$  twin boundaries, marked in red, next to the  $\{332\}<113>$  twin boundaries, were attributed to the mis-indexing of  $\alpha''$  martensite (Supplementary Figure 2) as confirmed in the TEM studies, Fig. 8b. The mis-indexing was attributed to a small lattice strain during  $\{0\bar{1}1\}<011>$  shuffles for the  $\beta$  to  $\alpha''$  transformation [33]. The small strain values results in a very small shape change, so the  $\alpha''$  crystal lattice is close to the  $\beta$  crystal lattice, such that the  $\alpha''$  EBSD Kikuchi pattern exhibits a pseudo-cubic symmetry [33,34]. A

similar phenomenon has previously been observed in Ti-36Nb-2Ta-3Zr [33]. Some of the  $\{332\}<113>$  twins in grain 1 propagated into neighbouring grains 2, 3 and 5, indicated by white arrows in Fig. 6b. The propagation of  $\{332\}<113>$  twins from one grain into another has previously been observed in Ti-12Mo [13] and Ti-15Mo-5Zr [35].

Profuse  $\{112\}<111>$  twinning was observed in grain 4, with martensite observed in the  $\{112\}<111>$  twins, as later confirmed by TEM analysis; most of the deformation bands in grain 4 could not be indexed. Only several fine deformation bands were indexed as  $\{112\}<111>$  twins and no propagation of  $\{332\}<113>$  twinning from grain 1 to grain 4 was observed. In grain 5, both  $\{112\}<111>$  twins and  $\{332\}<113>$  twins were observed. The kernel average misorientation (KAM) map [36], Fig. 6c, shows the local misorientation level (the higher KAM value, the higher the misorientation). Larger  $\{332\}<113>$  twins in grains 1–3 possessed higher KAM values and the interaction regions between  $\{332\}<113>$  twin variants gave rise to unindexable areas. In grains 4–5, the large (black) non-indexed deformation bands were  $\{112\}<111>$  twins containing martensite, confirmed by TEM below and Fig. 7. A BSE image of these non-indexed deformation bands is shown in Fig. 6d; nano-scale secondary bands were observed within these bands.

TEM analysis, Fig. 7, was conducted to understand the non-indexed deformation bands in Fig. 6. The  $\beta[113]$  zone axis SAED pattern from the interface between the left-hand side primary band and matrix is shown in Fig. 7d, confirming the presence of a  $\{112\}<111>$  twin,  $\alpha''$  martensite and  $\omega$ . Fig. 7b shows a DF image using the  $(101)_{\beta t}$  diffraction spot, confirming that the parallel primary deformation bands are  $\{112\}<111>$  twins. The DF image in Fig. 7c used the  $(111)_{\alpha''}$  diffraction spot, confirming that the secondary deformation bands in this  $\{112\}<111>$  twin are martensite. The



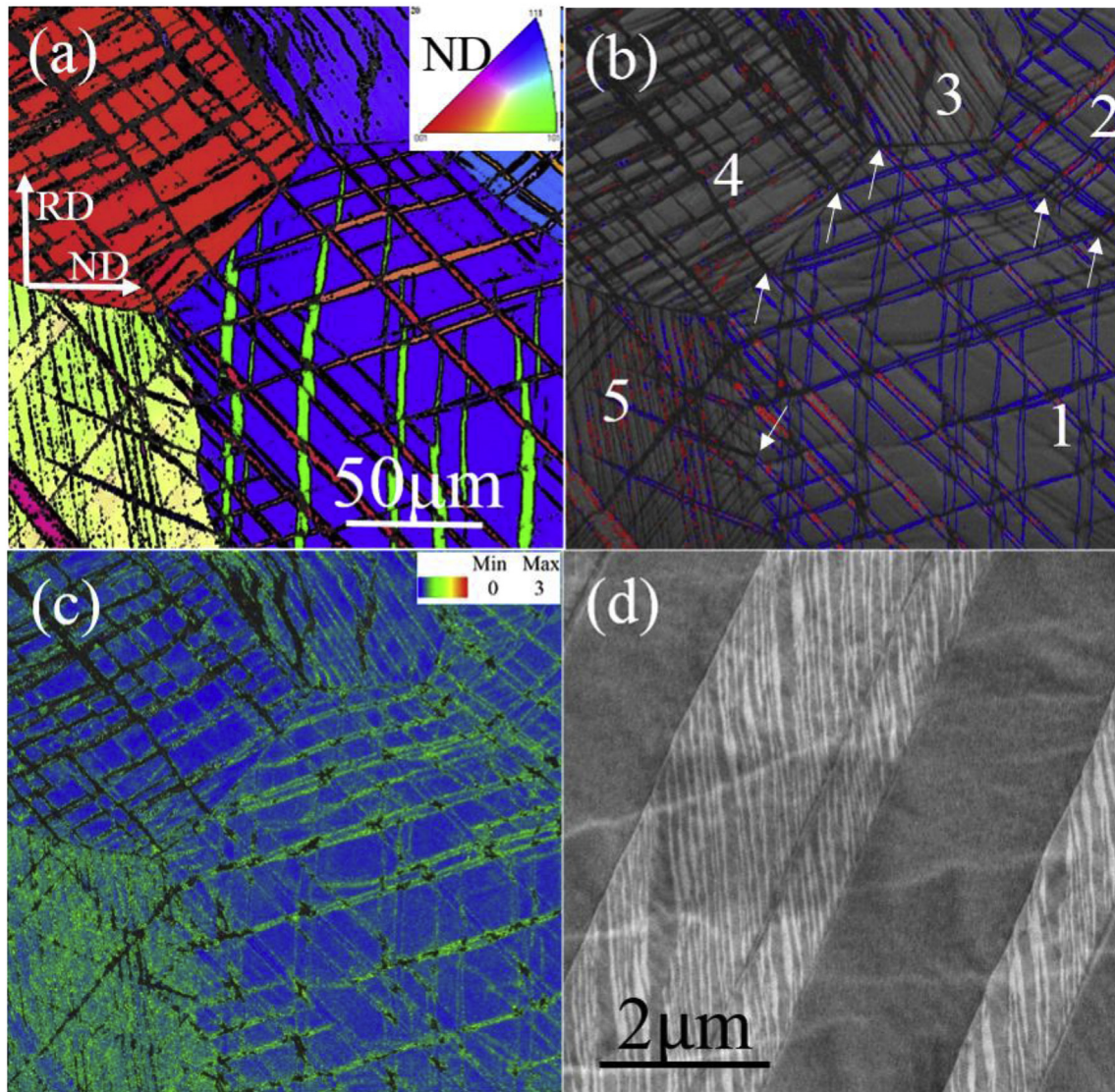


**Fig. 6.** EBSD analysis after 5% total tensile strain. (a) IPF map superimposed on a band contrast map. (b) Band contrast map superimposed with  $\{332\}\langle 113 \rangle$  twin boundaries in blue and  $\{112\}\langle 111 \rangle$  twin boundaries in red. (c) Kernel average misorientation map (for indexed areas, the higher misorientation level, the brighter green colour; non-indexed areas in black. (d) High magnification BSE image taken from a non-indexed band. (For interpretation of the references to colour in this figure legend, the reader is referred to the Web version of this article.)

mottling observed in Fig. 7b is  $\alpha''$  transformation induced planar complex of  $\omega$ , as suggested in Ref. [2].

A  $\{332\}\langle 113 \rangle$  twin in this sample was also studied, Fig. 8. The BF image in Fig. 8a shows that the deformation band was 870 nm in width and contained a high density of linear features that are tentatively identified as dislocations, highlighted by white arrows in Fig. 8a, as previously suggested [22,37–39]. The twinning was identified as  $\{332\}\langle 113 \rangle$  from the indexed  $\beta[011]$  zone axis SAED pattern. The SAED pattern in Fig. 8f confirms the presence of  $\beta$ ,  $\omega$  phase and  $\alpha''$  martensite in the  $\{332\}\langle 113 \rangle$  twin. Fig. 8b shows that the martensite predominantly occurred along the sides of the twin (highlighted by the red arrows), corresponding to the high KAM and mis-indexing of the  $\{332\}\langle 113 \rangle$  twins in Fig. 6. Fig. 8c–d shows the distribution of two of the  $\omega$  variants; this analysis is supported by the relative intensity of the two spots in the centre and edge of the twin, shown in Fig. 8g–h. Thus, variant  $\omega_1$  occurred mostly in the middle of the twin, while  $\omega_2$  occurred towards the twin boundaries.

Fig. 9 shows an example of secondary twinning in a  $\{332\}\langle 113 \rangle$  twin. Fig. 9a shows the DF image recorded using the  $(0\bar{1}1)_{st}$  diffraction spot in Fig. 9c, identifying the secondary deformation bands as  $\{112\}\langle 111 \rangle$  twins.

### 3.5. Microstructural analysis after 16% strain

The Ti-73 alloy with 16% strain was studied only by TEM because the EBSD index rate was insufficient due to the high strain/stress induced complex structure. Fig. 10 shows a  $\{112\}\langle 111 \rangle$  twin in the sample subjected to 16% total tensile strain. Two additional nano-scale bands were observed in the twin, Fig. 10a (BF) and b (DF), compared to the single twins found in the 5% strain sample (e.g. Fig. 7). The indexed SAED pattern, Fig. 10e recorded from the  $\{112\}\langle 111 \rangle$  twin and matrix confirms the formation of a  $\{112\}\langle 111 \rangle$  twin and two martensite variants with orientation relationship  $[13\bar{1}]_{\beta} // [\bar{1}\bar{1}2]_{\alpha''_1} // [\bar{1}\bar{1}2]_{\alpha''_2}$ . The DF images in Fig. 10c–d shows the distribution of  $\alpha''_1$  and  $\alpha''_2$ , respectively. Notably, the  $[\bar{1}\bar{1}2]_{\alpha''_1}$  variant

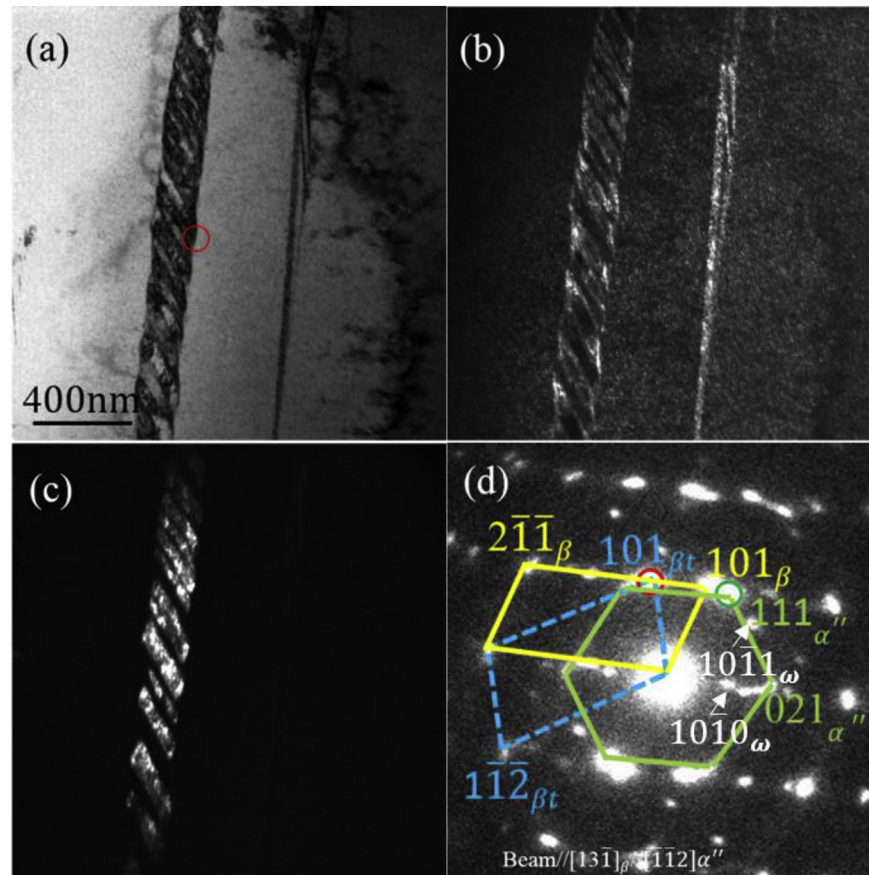


**Fig. 7.** TEM analysis after 5% total tensile strain. (a) BF image of two parallel deformation bands; secondary deformation bands were observed. (d)  $\beta$  [13 $\bar{1}$ ] zone axis SAED pattern recorded from the interface between the primary band and matrix (red circle in (a)). (b) DF image using (101)<sub>βt</sub> (red circle in (d)). (c) DF image recorded using (111)<sub>α''</sub> diffraction spot, green circle in (d). (For interpretation of the references to colour in this figure legend, the reader is referred to the Web version of this article.)

was grown at the twin interface, presumably induced symmetrically, associated with twinning shear and/or twinning dislocations.

Fig. 11 examines another area of the same sample and shows that the  $\beta$  matrix of three {112}<111> twins has almost completely transformed to martensite and that three martensite variants were observed at this strain. Fig. 11b presents the DF image recorded using (002)<sub>βt</sub>, showing that three {112}<111> twins were present. Fig. 11d–f shows the distributions of three martensite variants,  $\alpha''_{v1}$ ,  $\alpha''_{v2}$  and  $\alpha''_{v3}$ , respectively. Fig. 11c shows that the matrix marked by the dashed line in Fig. 11b transformed mostly to variant  $\alpha''_{v1}$ . As shown in Fig. 11f, only one set of diffraction spots corresponding to the  $\beta$  were observed. Secondary nanoscale parallel  $\alpha''_{v1}$  variant with a width around 45 nm was observed in the bottom  $\beta$  phase (Fig. 11d) within the {112}<111> twin. Fig. 11d shows that  $\alpha''_{v2}$  mainly occurred in the {112}<111> twin. The bright particles observed in the  $\beta$  phase in the lower region of Fig. 11d may be  $\omega$  phase; as can be observed in SAED pattern (Fig. 11e), the diffraction spots of ( $\bar{1}$ 010) $\omega$  were very close to (00 $\bar{1}$ ) $\alpha''_{v2}$ . Fig. 11e shows the distribution of  $\alpha''_{v3}$ , which was mainly adjacent to the twin. The SAED pattern confirms the formation of three martensite variants, which share an orientation relationship ( $\bar{1}$ 10) $\beta$  // ( $\bar{1}$ 01) $\alpha''_{v1}$  // (10 $\bar{1}$ ) $\alpha''_{v2}$  // (020) $\alpha''_{v3}$ .

Fig. 12 shows the formation of individual quadrilaterals of martensite at the intersection regions of two series of high density {112}<111> twin variants. In the bright field image, (a), the edges of the dark quadrilaterals inscribe an acute angle of 34.2°, which is very close to the acute angle of 33.5° between the two {112}<111> twinning planes, (2 $\bar{1}\bar{1}$ ) and (1 $\bar{1}\bar{2}$ ) on the [13 $\bar{1}$ ]<sub>β</sub> zone axis. The dark

field analysis indicates that the quadrilaterals are in the twinned orientation (c) rather than that of the matrix (b), and contain martensite (d) with orientation relationship [13 $\bar{1}$ ]<sub>β</sub> // [1 $\bar{1}\bar{2}$ ]<sub>α''</sub>. Thus, the repeated shear cause by secondary twinning appears to be particularly effective at inducing martensite formation.

#### 4. Discussion

##### 4.1. Effect of grain size on deformation heterogeneity during the early stages of plasticity

In the early stages of plasticity (1.3% total strain, 0.2% plastic strain), plasticity occurred mostly in large grains and by a combination of twinning and dislocation glide (Supplementary Figure1). Moreover, martensite was not observed at this strain. Therefore, the high initial work hardening rate can be attributed to twinning, since dislocation glide in  $\beta$  Ti is not usually found to produce work hardening. No evidence for stress-induced  $\alpha''$  martensite formation was found. The formation of  $\alpha''$  produces superelasticity but not significant work hardening (see also, for comparison, examples in Ti-10V-3Fe-3Al [19] and Ti-Nb alloys [4,20]). Heterogeneity of deformation between  $\beta$  grains with different twinning stresses due to both grain sizes and orientation may also be important in producing hardening during the early stages plasticity, e.g. load transfer between grains.

In order to examine these issues, we turn to the EBSD and TEM analysis (Figs. 4–5) of this sample. These show that both {332}<113> and {112}<111> twinning were activated. The {332}<113>



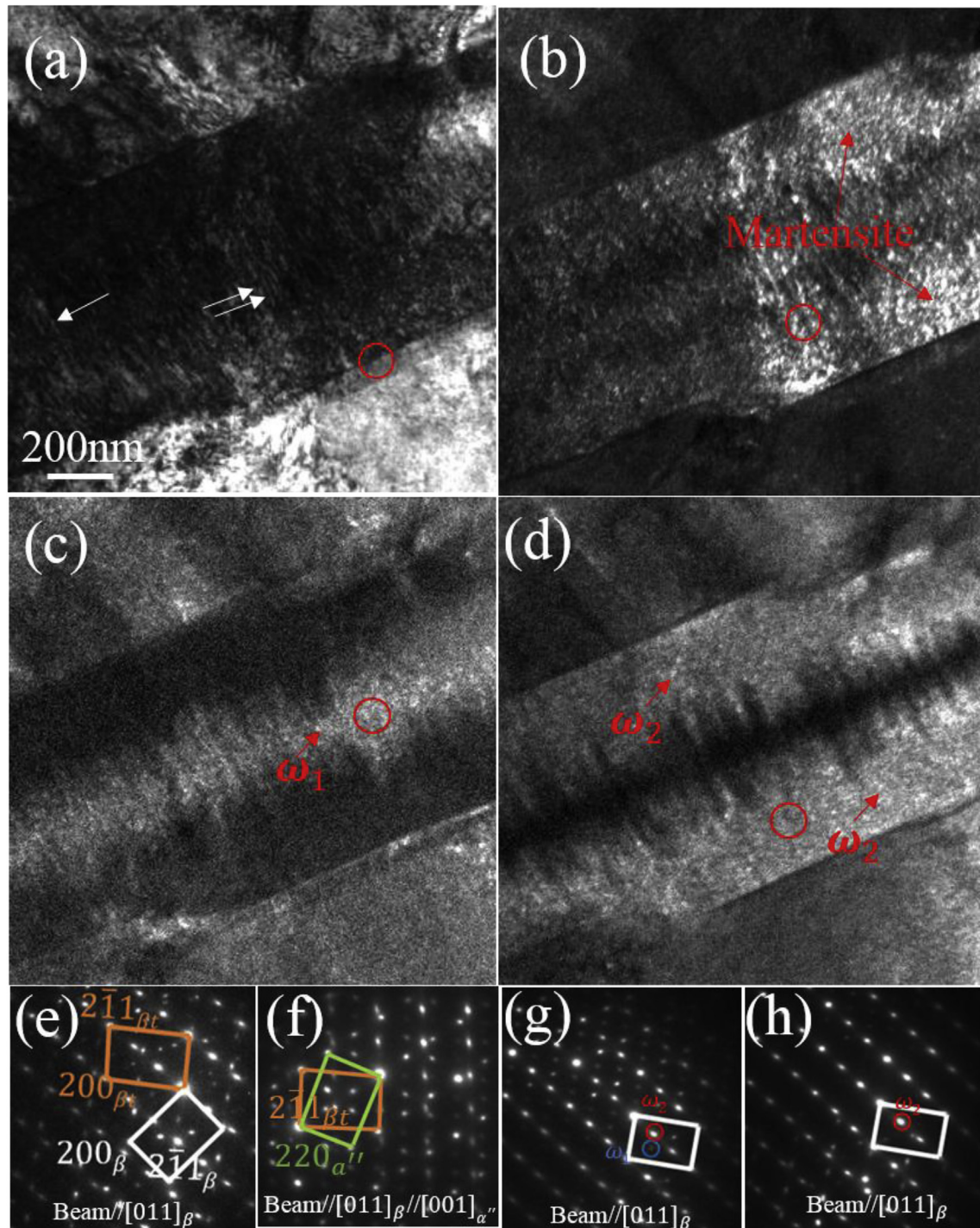


**Fig. 8.** TEM analysis of {332}<113> twin in sample after 5% tensile strain. (a) BF image of the deformation band and the white arrow highlighted linear features are dislocations. (b) DF image recorded using the  $(\bar{1}10)_{a''}$  diffraction spot, red circle in (f). The bright regions highlighted by the red arrow are martensite. (c) and (d) DF images using the blue ( $\omega_1$ ) and red ( $\omega_2$ ) diffraction spots in (g). (e)–(h) SAED patterns from the regions marked with red circles in (a)–(d), respectively. (For interpretation of the references to colour in this figure legend, the reader is referred to the Web version of this article.)

twins were only observed in the largest grain in Fig. 4b. This is reasonable because, for most cases, the twinning stress ( $\sigma_T$ ) obeys the Hall-Petch relationship ( $\sigma_T = \sigma_{T0} + K_T d^{-1/2}$ ) [40–42]. Of course, in addition to the grain size, the resolved shear stress on the twin plane would be expected also to control the activation of twinning in an individual grain [12,35]. Table 2 shows the {332}<113> twin variants with an absolute SF value above 0.3 for grains

1, 2 and 3 in Fig. 4. The {332}<113> twin variant in grain 1 with the highest positive SF is  $(332)[11\bar{3}]$ , with a SF of 0.444, while for grain 2, the {332}<113> twin variants with the highest positive SF is  $(332)[11\bar{3}]$ , with a SF of 0.488. For grain 3,  $(332)[11\bar{3}]$  and  $(2\bar{3}3)[\bar{3}11]$  share a positive SF of 0.457. Although the SF for the  $(3\bar{3}2)[11\bar{3}]$ ,  $(332)[11\bar{3}]$  and  $(2\bar{3}3)[\bar{3}11]$  twin variants in grains 2 and 3 was 0.488 and 0.457, which are higher than that of 0.444 for  $(332)[11\bar{3}]$

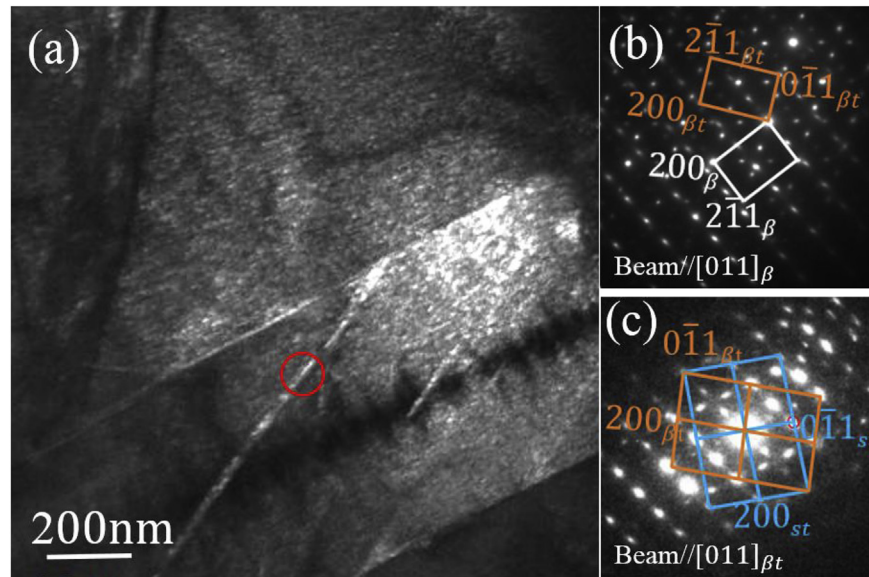


**Fig. 9.** TEM analysis of secondary twinning inside a different region of the  $\{332\}\langle 113 \rangle$  twin in Fig. 8, in the 5% tensile strain sample. (a) DF image recorded using  $(011)_{st}$  diffraction spot, red circle in (c). (b) SAED pattern from the interface between the primary deformation band and the matrix. (c) SAED pattern recorded marked region by the red circle in (a). (For interpretation of the references to colour in this figure legend, the reader is referred to the Web version of this article.)

observed in grain 1, no  $\{332\}\langle 113 \rangle$  twin variant was activated in grains 2 and 3. Therefore, grain size can be inferred to affect the activation of  $(\bar{3}\bar{3}2)[\bar{1}\bar{1}\bar{3}]$  twinning, as expected, leading to heterogeneous deformation between larger grains and smaller grains.

The heterogeneous deformation between larger and smaller grains is beneficial to the high strain hardening rate, as extensively studied in bimodal alloys with micrometer-sized grains randomly embedded among much finer grains structures [43,44]. The larger grains would be expected to preferentially accommodate strains at yield. However, twinning also occurred preferentially in the larger grains, providing barriers to dislocation motion. This effectively sub-dividing grains, such that the larger grains would have hardened to the point at which the finer grains yielded.

#### 4.2. Higher dynamic strain hardening behaviour because of the SF governed twin system selection

Table 3 shows the SF of twin variants possessing an absolute value above  $\pm 0.3$  of both  $\{332\}\langle 113 \rangle$  and  $\{112\}\langle 111 \rangle$  type twinning for grains 1, 2, 4 and 5 in Fig. 6. In grain 1, there was only one  $\{112\}\langle 111 \rangle$  twin variant,  $(2\bar{1}\bar{1})[\bar{1}11]$ , with an absolute value of SF ( $-0.40$ ) above  $\pm 0.3$ , but because the value of the SF was negative, activation was not possible in tension. By contrast, there were three  $\{332\}\langle 113 \rangle$  twin variants with a positive SF above 0.3 in grain 1, and therefore  $\{332\}\langle 113 \rangle$  twinning was activated. In grain 4, four  $(2\bar{1}\bar{1})[\bar{1}11]$  twin variants possessed a positive SF above 0.3, two with a SF of 0.49,  $(2\bar{1}\bar{1})[\bar{1}11]$  and  $(211)[\bar{1}\bar{1}\bar{1}]$ , whilst all the  $\{332\}\langle 113 \rangle$  twin variants possessed negative Schmid factors in grain 4, and therefore only the  $(2\bar{1}\bar{1})[\bar{1}11]$  twin system was observed. In grain 5, both the  $(2\bar{1}\bar{1})[\bar{1}11]$  and  $\{332\}\langle 113 \rangle$  twin systems possessed variants with positive SF above 0.3, with two being very similar in magnitude:  $(2\bar{1}\bar{1})[\bar{1}11]$  0.41 and  $(\bar{3}\bar{3}2)[\bar{1}\bar{1}\bar{3}]$  0.42. Since the critical resolved shear stress for  $\{112\}\langle 111 \rangle$  twinning is slightly lower (but very close) to that of the  $\{332\}\langle 113 \rangle$  twinning system [12], both twin systems were activated in grain 5. In order to make the SF analysis more statistically meaningful, another 16 grains were analysed (Supplementary Figure 3 and Supplementary Table 1). This analysis suggests that twin system selection in individual grains is mainly governed by the Schmid factor, over and above

phase stability. No dominant twin system was found, and the  $\{332\}\langle 113 \rangle$  and  $\{112\}\langle 111 \rangle$  systems occurred in approximately equal amounts in this Ti-73 alloy (Supplementary Figure 3 and Supplementary Table 1). Therefore, there was a greater potential for twinning to occur for individual grains with different orientations and grain size. This led to a higher dynamic strain hardening behaviour than TWIP alloys that exhibit a single or one dominant twin system such as Ti-15Mo [25] and Ti-10Mo-1Fe [26].

#### 4.3. Significant strain hardening contributions of nanotwins and nanoscale martensite in twins and secondary twins

Each mechanical twin traverses a grain, resulting in a decrease of the dislocation mean free path, which is termed the dynamic Hall-Petch mechanism [25]. Therefore, both  $\{112\}\langle 111 \rangle$  and  $\{332\}\langle 113 \rangle$  twinning have the potential to contribute to work hardening, providing a conceptual route to the development of new metastable  $\beta$  titanium alloys that resist necking and therefore show enhanced ductility. Recently, the dynamic strain hardening effects of  $\{332\}\langle 113 \rangle$  twinning have been discussed in Ti-Nb [45] and Ti-15Mo [25] alloys as  $\{112\}\langle 111 \rangle$  twinning was the dominant deformation mechanism in these alloys. In order to understand the underlying strain hardening mechanisms of this Ti-73 alloy, quantitative evaluation of the straining hardening effects of the  $\{112\}\langle 111 \rangle$  and  $\{332\}\langle 113 \rangle$  twin systems was conducted in EBSD scale of the alloy with 5% strain. We assume that the strength  $\sigma$  can be defined as [46]:

$$\sigma = \sigma_0 + \Delta\sigma_f + \Delta\sigma_t \quad (1)$$

where  $\sigma_0$  is the intrinsic (lattice friction) strength to move a dislocation including solid solution hardening,  $\Delta\sigma_f$  is the isotropic hardening contribution from forest dislocations and  $\Delta\sigma_t$  is the flow stress increment from  $\{112\}\langle 111 \rangle$  or  $\{332\}\langle 113 \rangle$  twinning.  $\Delta\sigma_t$  can be expressed [45,47]:

$$\Delta\sigma_t = M\beta Gb/\lambda \quad (2)$$

where  $\beta$  is the Taylor constant of 0.5 [48] and  $G$  is the material shear



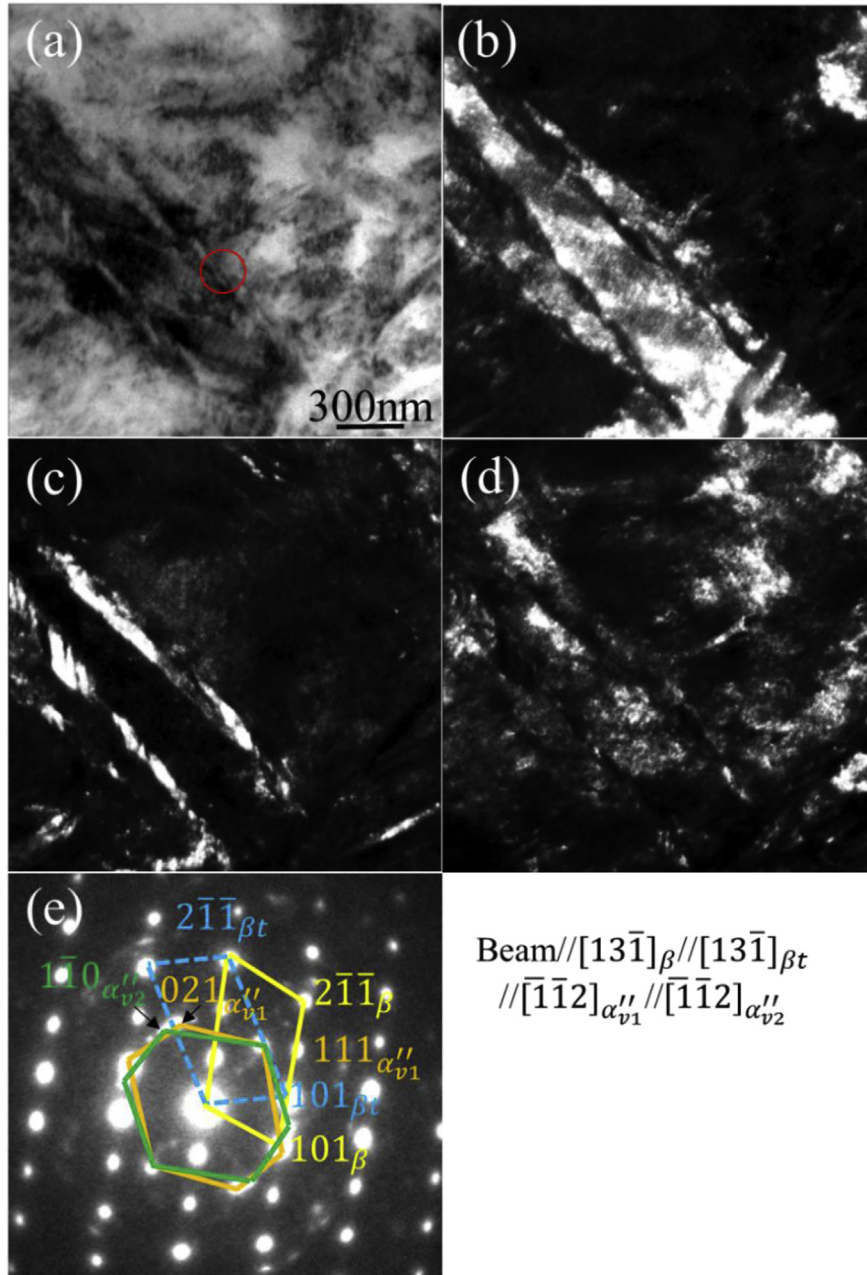


**Fig. 10.** TEM analysis after tensile straining to 16% total strain. (a) BF image, (b)–(d) DF images recorded using the  $(\bar{1}10)_{\beta t}$ ,  $(021)_{\alpha'v1}$  and  $(1\bar{1}0)_{\alpha'v2}$  spot in (e) the indexed SAED pattern from red circle marked area in (a). (For interpretation of the references to colour in this figure legend, the reader is referred to the Web version of this article.)

modulus which is around 36 GPa for this Ti-73 alloy.  $M$  is an average Taylor factor of 3.06 [45] and  $b$  is the magnitude of the Burgers vector of  $2.54 \times 10^{-10}$  m [45].  $\lambda$  is the dislocation mean free path [25,45]:

$$1/\lambda = 1/L + 1/D \quad (3)$$

where  $L$  is the grain size and  $D$  is the mean twin spacing, which can be calculated using the volume fraction  $f$  and twin thickness  $d$ :

$$1/D = f/[2d(1 - f)] \quad (4)$$

The volume fraction  $f$  of both  $\{112\}<111>$  and  $\{332\}<113>$  type twinning was approximated from the area fraction obtained by EBSD of the Ti-73 alloy with 5% strain. Grains for each twin system

were selected under the following two conditions: (i) with comparable grain size in the range between 100 and 150  $\mu\text{m}$ ; (ii) with at least three twin variants of  $\{112\}<111>$  or  $\{332\}<113>$  with positive SF above 0.3. Note that nanoscale features such as nanotwins, martensite and  $\omega$  phase transformation in both  $\{112\}<111>$  and  $\{332\}<113>$  twinning was not considered in this evaluation. The area fraction for the  $\{112\}<111>$  twin was 36.5%, measured using the EBSD results covering an area  $>100000 \mu\text{m}^2$  and  $d$  is 0.6  $\mu\text{m}$ , which is taken as half of the average twin width based on stereological relations [25]. The area fraction for  $\{112\}<111>$  twin is 32.5% and  $d$  is 1.0  $\mu\text{m}$ . All these values are summarized in Table 4. Substituting into equations (2)–(4),  $\Delta\sigma_t$  for  $\{112\}<111>$  and  $\{332\}<113>$  twinning is 6.9 MPa and 3.6 MPa, respectively. These values are too low for the twins detected by EBSD to be the dominating



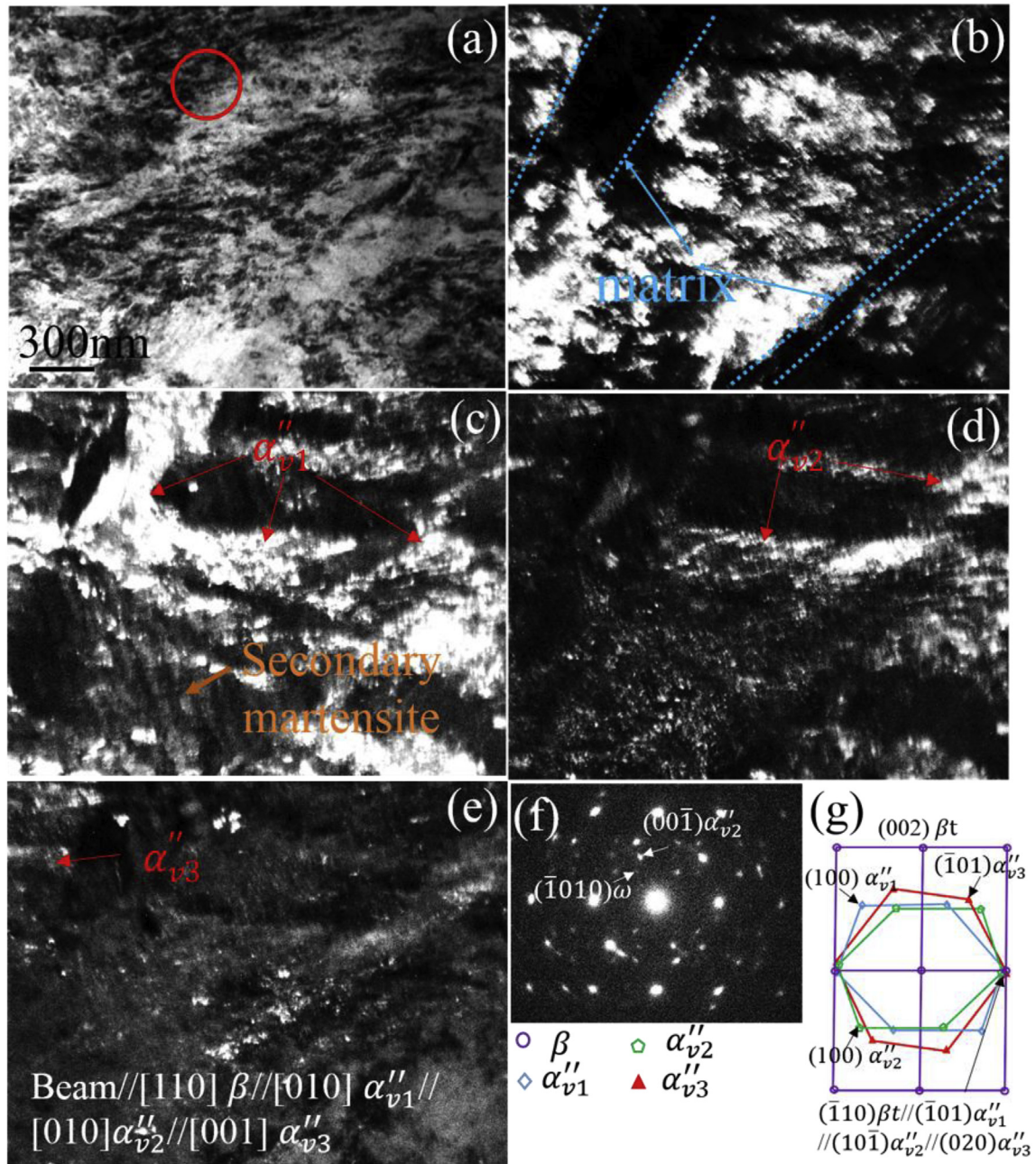


**Fig. 11.** Further TEM analysis sample subject to 16% total tensile strain. (a) BF image. (b) DF image recorded using (002) $\beta t$ . (c)–(e) DF images recorded using (100) $\alpha''_{v1}$ , (001) $\alpha''_{v2}$  and (101) $\alpha''_{v3}$ , respectively. (f) SAED pattern recorded from the red circle in (a), and (g) its indexed corresponding key diagram. (For interpretation of the references to colour in this figure legend, the reader is referred to the Web version of this article.)

contribution to the observed strain hardening behaviour.

The disparity between the calculated  $\Delta\sigma_t$  for {112}<111> and {332}<113> twinning and the observed strain hardening levels must therefore be inferred to be due to the contribution of the nano-scale twins (Fig. 5), nano-scale martensite observed in both {112}<111> (Fig. 7) and {332}<113> (Fig. 8) twins and the secondary twinning in {332}<113> twins (Fig. 9), all of which were below the spatial resolution of the EBSD measurements. A reasonable  $\Delta\sigma_t$  (99 MPa) can be obtained for {112}<111> twinning if the twin thickness is taken as 80 nm (Table 4), half the width of the high density parallel {112}<111> twins (~160 nm in Fig. 5), which is reasonable given the large quantity of nano-scale parallel {112}<111> twins observed by TEM. From the stress-strain curve

(Fig. 3), the stress increased by 89 MPa from yielding (707 MPa) to 5% strain (796 MPa), which matches reasonably with the  $\Delta\sigma_t$  (49.7 MPa) calculated for the {112}<111> twin. Thus, this shows that the contributions to strain hardening cannot be rationalised purely by EBSD measurements, rather TEM is required.

#### 4.4. Deformation mechanism

Fig. 13 shows the microstructural evolution of the Ti-73 alloy with an increase of strain, which exhibits markedly different deformation mechanisms in the initial deformation stage compared to metastable  $\beta$  titanium alloys with both TRIP and TWIP effects, as referred in Fig. 10 in Ref. [13]. The initial deformation

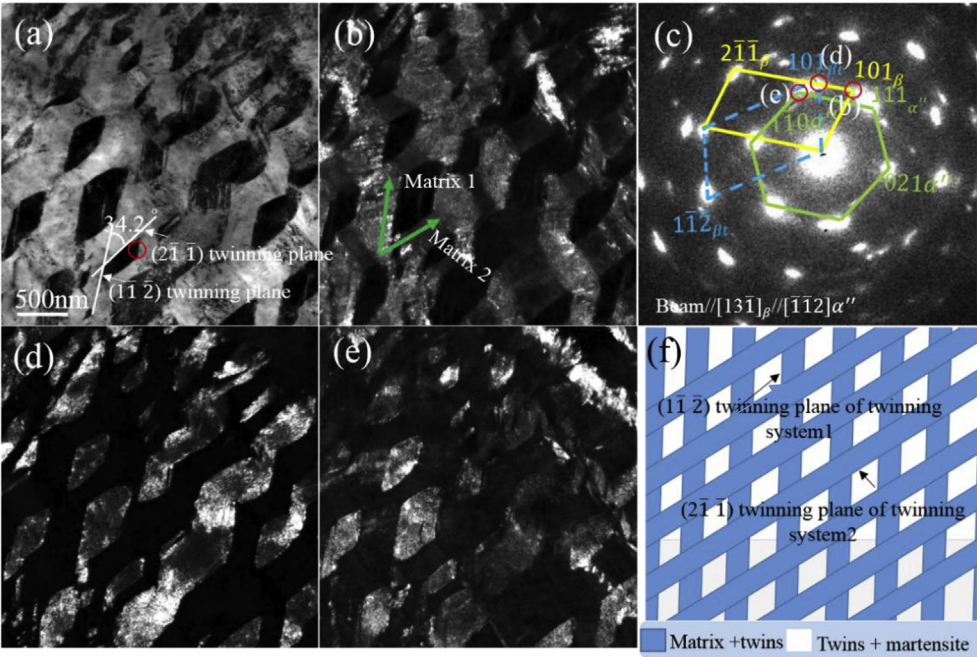


**Fig. 12.** Further TEM analysis of the sample deformed to 16% strain. (a) BF image and its SAED pattern (c) recorded from the interface, red circle marked region in (a). (b)–(e) DF images recorded the marked diffraction spots  $(101)_{\beta}$ ,  $(101)_{\beta t}$  and  $(110)_{\alpha'}$ , respectively, indicated in the SAED pattern (c). (f) Schematic diagram of the proposed formation mechanism. (For interpretation of the references to colour in this figure legend, the reader is referred to the Web version of this article.)

**Table 4**  
Numerical values of physical constants and of the identified parameters.

$\beta$ , Taylor constant	0.5
G, shear modulus (Ti-73)	36 GPa
M, average Taylor factor	3.06
b, Burgers vector	$2.54 \times 10^{-10}$ m
$\lambda$ dislocation mean free path	EBSD level $\{112\}\langle 111 \rangle$ 2.08 $\mu\text{m}$
	EBSD level $\{332\}\langle 113 \rangle$ 4.16 $\mu\text{m}$
	TEM level Parallel $\{112\}\langle 111 \rangle$ twin 0.278 $\mu\text{m}$

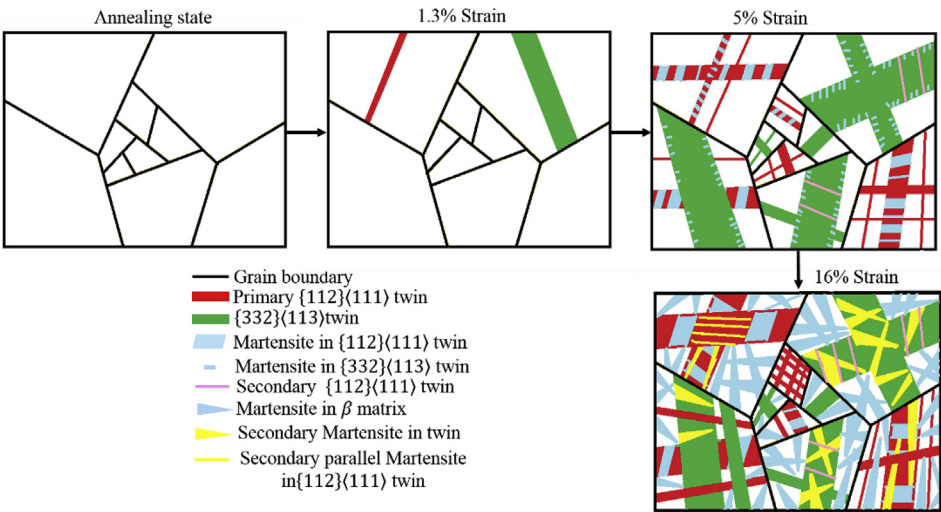


**Fig. 13.** Schematic illustration of the microstructural evolution of the Ti-73 alloy with an increase of strain. The activation of different deformation mechanisms is shown from annealing state to the strain (16%) around the highest strain hardening rate.



mechanisms of metastable  $\beta$  titanium alloys with both TRIP and TWIP effects is usually martensite transformation and primary  $\{332\}\langle 113 \rangle$  twinning [13]. As expected from the design intent, the initial deformation mechanisms of the Ti-73 alloy were  $\{332\}\langle 113 \rangle$  (Fig. 4),  $\{112\}\langle 111 \rangle$  twinning (Fig. 5) and the absence of martensite transformation due to the increased  $\beta$  phase stability. Both the suppressed stress-induced martensite transformation and the formation of athermal  $\omega$  contributed to the high yield strength and the absence of a stress plateau. Sun et al. suggested that the athermal  $\omega$  precipitate/matrix interface maintains a high degree of coherency, which results in elastic strain fields and consequent hardening of the surrounding  $\beta$  matrix, leading to an increase of yield strength [18]. The high strain hardening rate after yield was attributed to the heterogeneous deformation between large grains and small grains, the absence of stress-induced martensite transformation and the activation of both  $\{332\}\langle 113 \rangle$  and  $\{112\}\langle 111 \rangle$  twinning with neither being evidently dominant, which contributes more twinning choices for individual grains.

As discussed in section 4.2, the SF dominates the selection of the twin system between  $\{332\}\langle 113 \rangle$  and  $\{112\}\langle 111 \rangle$ . It has been reported that in metastable  $\beta$  Ti alloys, with an increase of  $\beta$  phase stability, the activated twinning system shifts from  $\{332\}\langle 113 \rangle$  to  $\{112\}\langle 111 \rangle$  [13,22,49–52]. Since both systems were observed here, with neither being evidently dominant, this suggests that the chemical composition of Ti-7Mo-3Cr is around the transition between  $\{332\}\langle 113 \rangle$  and  $\{112\}\langle 111 \rangle$  twinning. Therefore, twin system selection is dominated by the Schmid factor. In Figs. 7–9, secondary deformation products such as martensite or secondary twinning were observed in the primary twins after 5% strain. As reported in Refs. [12,13], the twinned  $\beta$  zone exhibits a modified orientation factor in comparison with the matrix. The activation of secondary twinning or martensite in the primary twins upon further straining depends on the modified orientation factor of the secondary twinning plane [12,13]. The stabilized high strain hardening rate (around 1600 MPa) between 5% and 10% strain was attributed to  $\{332\}\langle 113 \rangle$  and  $\{112\}\langle 111 \rangle$  twinning with neither being evidently dominant, martensite and  $\omega$  phase transformations within these two types of twins, and the formation of secondary twins in  $\{332\}\langle 113 \rangle$  type twins, according to the calculation in 4.3.

The TEM results (Figs. 10–12) show that beyond 10% strain, the increase of strain hardening rate can be attributed to the formation of new nanoscale martensite variants in both  $\{112\}\langle 111 \rangle$  twins and the matrix, the formation of secondary nanoscale martensite in the remaining  $\beta$  phase in the  $\{112\}\langle 111 \rangle$  twins, and twin-twin interaction between two sets of high density parallel  $\{112\}\langle 111 \rangle$  twins. In metastable  $\beta$  titanium alloys with both TRIP and TWIP effects, primary micrometer scale martensite was formed in the matrix during yielding. However, in this Ti-73 alloy, extensive nanometre scale martensite formation in the matrix was significantly postponed to a strain between 10% and 16%, correlating to the “bump” on the strain hardening curve in Fig. 3. Considering the activation of primary and secondary products depends on the orientation factors of matrix and twins [12,13,52], it is reasonable to see more deformation products with an increase of stress/strain, as less favoured twinning and martensite variants could be activated, e.g. due to the grain rotation during straining and the requirement to maintain continuity between the grains. Yang et al. [53] and Meng et al. [54] found that in TWIP steels, grains rotate towards 111//tensile axis during tension, which renders the crystals favourably oriented for twinning. Moreover, it is also reported that at high strain state, the twinning activity is controlled by local stress state instead of simply grain orientation, because the local stress state may be very different from the macroscopic stress state [42].

## 5. Conclusions

In this work, by shifting the deformation mechanisms from martensite transformation to  $\{332\}\langle 113 \rangle$  and  $\{112\}\langle 111 \rangle$  twinning, a new metastable  $\beta$  titanium alloy with high strength and high strain hardening rate was developed. The heterogeneous deformation between large grains and small grains, the activation of both  $\{332\}\langle 113 \rangle$  and  $\{112\}\langle 111 \rangle$  with neither being evidently dominant, and the absence of stress-induced martensite transformation produced a high yield strength and high strain hardening rate, which successfully addressed the drawback of low yield strength of  $\beta$  titanium alloy with both TRIP and/or TWIP effects and poor strain hardening of TWIP metastable  $\beta$  titanium alloy. Twin system selection within grains was observed to depend upon Schmid factor, which shows that there was no dominant twinning system in this alloy. The strain hardening rate of ~1600 MPa between 5% and 10% strain was attributed, via a quantitative analysis, to the formation of  $\{332\}\langle 113 \rangle$  and  $\{112\}\langle 111 \rangle$  twins, orthorhombic  $\alpha''$  martensite and  $\omega$  phase within these two types of twins and the formation of secondary twins within the  $\{332\}\langle 113 \rangle$  twins. With further increase of strain to 16% total strain, the formation of new martensite variants occurred in both  $\{112\}\langle 111 \rangle$  twins and matrix. The formation of secondary nanoscale martensite in the remaining  $\beta$  phase in the  $\{112\}\langle 111 \rangle$  twins, and twin-twin interactions of two series of high density parallel  $\{112\}\langle 111 \rangle$  twins were observed.

## Acknowledgements

The authors gratefully acknowledge funding by the UK EPSRC under the DARE Programme Grant, EP/L025213/1. Helpful discussions and the assistance of Dr KM Rahman at Imperial College are also acknowledged.

## Appendix A. Supplementary data

Supplementary data related to this article can be found at <https://doi.org/10.1016/j.actamat.2018.04.035>.

## References

- [1] A. Devaraj, V.V. Joshi, A. Srivastava, S. Manandhar, V. Moxson, V.A. Duz, C. Lavender, A low-cost hierarchical nanostructured beta-titanium alloy with high strength, *Nat. Commun.* 7 (2016) 11176.
- [2] J. Zhang, C.C. Tasan, M.J. Lai, A.C. Dippel, D. Raabe, Complexion-mediated martensitic phase transformation in Titanium, *Nat. Commun.* 8 (2017) 14210.
- [3] A. Biesiekierski, J. Wang, M. Abdel-Hady Gepreel, C. Wen, A new look at biomedical Ti-based shape memory alloys, *Acta Biomater.* 8 (2012) 1661–1669.
- [4] H.Y. Kim, Y. Ikehara, J.I. Kim, H. Hosoda, S. Miyazaki, Martensitic transformation, shape memory effect and superelasticity of Ti-Nb binary alloys, *Acta Mater.* 54 (2006) 2419–2429.
- [5] G. Bolat, D. Mareci, R. Chelariu, J. Izquierdo, S. González, R.M. Souto, Investigation of the electrochemical behaviour of TiMo alloys in simulated physiological solutions, *Electrochim. Acta* 113 (2013) 470–480.
- [6] S.L. Raghunathan, R.J. Talling, D. Dye, Micromechanics, microstrains, and modelling of alpha, alpha-beta, and metastable beta Ti alloys, *J. Strain Anal. Eng. Des.* 45 (2010) 337–350.
- [7] M. Jackson, N.G. Jones, D. Dye, R.J. Dashwood, Effect of initial microstructure on plastic flow behaviour during isothermal forging of Ti-10V-2Fe-3Al, *Mater. Sci. Eng. A* 501 (2009) 248–254.
- [8] M. Abdel-Hady, K. Hinoshita, M. Morinaga, General approach to phase stability and elastic properties of  $\beta$ -type Ti-alloys using electronic parameters, *Scripta Mater.* 55 (2006) 477–480.
- [9] L.F. Huang, B. Grabowski, J. Zhang, M.J. Lai, C.C. Tasan, S. Sandlöbes, D. Raabe, J. Neugebauer, From electronic structure to phase diagrams: a bottom-up approach to understand the stability of titanium-transition metal alloys, *Acta Mater.* 113 (2016) 311–319.
- [10] D. Banerjee, J.C. Williams, Perspectives on titanium science and technology, *Acta Mater.* 61 (2013) 844–879.
- [11] X. Yang, C.R. Hutchinson, Corrosion-wear of  $\beta$ -Ti alloy TMZF (Ti-12Mo-6Zr-2Fe) in simulated body fluid, *Acta Biomater.* 42 (2016) 429–439.



- [12] E. Bertrand, P. Castany, I. Péron, T. Gloriant, Twinning system selection in a metastable  $\beta$ -titanium alloy by Schmid factor analysis, *Scripta Mater.* 64 (2011) 1110–1113.
- [13] F. Sun, J.Y. Zhang, M. Marteleur, T. Gloriant, P. Vermaut, D. Laillé, P. Castany, C. Curfs, P.J. Jacques, F. Prima, Investigation of early stage deformation mechanisms in a metastable  $\beta$  titanium alloy showing combined twinning-induced plasticity and transformation-induced plasticity effects, *Acta Mater.* 61 (2013) 6406–6417.
- [14] M. Marteleur, F. Sun, T. Gloriant, P. Vermaut, P.J. Jacques, F. Prima, On the design of new  $\beta$ -metastable titanium alloys with improved work hardening rate thanks to simultaneous TRIP and TWIP effects, *Scripta Mater.* 66 (2012) 749–752.
- [15] D. Kuroda, M. Niinomi, M. Morinaga, Y. Kato, T. Yashiro, Design and mechanical properties of new  $\beta$  type titanium alloys for implant materials, *Mater. Sci. Eng. A* 243 (1998) 244–249.
- [16] F. Sun, J.Y. Zhang, M. Marteleur, C. Brozek, E.F. Rauch, M. Veron, P. Vermaut, P.J. Jacques, F. Prima, A new titanium alloy with a combination of high strength, high strain hardening and improved ductility, *Scripta Mater.* 94 (2015) 17–20.
- [17] T. Yao, K. Du, H. Wang, Z. Huang, C. Li, L. Li, Y. Hao, R. Yang, H. Ye, In situ scanning and transmission electron microscopy investigation on plastic deformation in a metastable  $\beta$  titanium alloy, *Acta Mater.* 133 (2017) 21–29.
- [18] F. Sun, J.Y. Zhang, P. Vermaut, D. Choudhuri, T. Alam, S.A. Mantri, P. Svec, T. Gloriant, P.J. Jacques, R. Banerjee, F. Prima, Strengthening strategy for a ductile metastable  $\beta$ -titanium alloy using low-temperature aging, *Mater. Res. Lett.* 5 (2017) 547–553.
- [19] M. Ahmed, D. Wexler, G. Casillas, D.G. Savvakis, E.V. Pereloma, Strain rate dependence of deformation-induced transformation and twinning in a metastable titanium alloy, *Acta Mater.* 104 (2016) 190–200.
- [20] Y. Yang, S.Q. Wu, G.P. Li, Y.L. Li, Y.F. Lu, K. Yang, P. Ge, Evolution of deformation mechanisms of Ti–22.4Nb–0.73Ta–2Zr–1.340 alloy during straining, *Acta Mater.* 58 (2010) 2778–2787.
- [21] H. Xing, J. Sun, Mechanical twinning and omega transition by  $\langle 111 \rangle$  {112} shear in a metastable  $\beta$  titanium alloy, *Appl. Phys. Lett.* 93 (2008), 031908.
- [22] S. Hanada, O. Izumi, Correlation of tensile properties, deformation modes, and phase stability in commercial  $\beta$ -phase titanium alloys, *Metall. Mater. Trans.* 18 (1987) 265–271.
- [23] Y.L. Hao, S.J. Li, S.Y. Sun, C.Y. Zheng, R. Yang, Elastic deformation behaviour of Ti–24Nb–4Zr–7.95Sn for biomedical applications, *Acta Biomater.* 3 (2007) 277–286.
- [24] H. Liu, M. Niinomi, M. Nakai, J. Hieda, K. Cho, Changeable Young's modulus with large elongation-to-failure in  $\beta$ -type titanium alloys for spinal fixation applications, *Scripta Mater.* 82 (2014) 29–32.
- [25] X. Min, X. Chen, S. Emura, K. Tsuchiya, Mechanism of twinning-induced plasticity in  $\beta$ -type Ti–15Mo alloy, *Scripta Mater.* 69 (2013) 393–396.
- [26] X.H. Min, S. Emura, T. Nishimura, K. Tsuchiya, K. Suzuki, Tensile deformation mode and crevice corrosion resistance in Ti–10Mo–xFe alloys, *Mater. Sci. Eng. A* 527 (2010) 5499–5506.
- [27] X. Zhao, M. Niinomi, M. Nakai, G. Miyamoto, T. Furuhashi, Microstructures and mechanical properties of metastable Ti–30Zr–(Cr, Mo) alloys with changeable Young's modulus for spinal fixation applications, *Acta Biomater.* 7 (2011) 3230–3236.
- [28] P. Majumdar, S.B. Singh, M. Chakraborty, Elastic modulus of biomedical titanium alloys by nano-indentation and ultrasonic techniques—a comparative study, *Mater. Sci. Eng. A* 489 (2008) 419–425.
- [29] A. Devaraj, S. Nag, R. Srinivasan, R.E.A. Williams, S. Banerjee, R. Banerjee, H.L. Fraser, Experimental evidence of concurrent compositional and structural instabilities leading to  $\omega$  precipitation in titanium–molybdenum alloys, *Acta Mater.* 60 (2012) 596–609.
- [30] M.J. Lai, C.C. Tسان, D. Raabe, H.L. Fraser, Experimental evidence of concurrent compositional and structural instabilities leading to  $\omega$  precipitation in titanium–molybdenum alloys, *Acta Mater.* 100 (2015) 290–300.
- [31] M.J. Lai, C.C. Tسان, J. Zhang, B. Grabowski, L.F. Huang, D. Raabe, Origin of shear induced  $\beta$  to  $\omega$  transition in Ti–Nb-based alloys, *Acta Mater.* 92 (2015) 55–63.
- [32] H. Xing, J. Sun, Mechanical twinning and omega transition by  $\langle 111 \rangle$  {112} shear in a metastable  $\beta$  titanium alloy, *Appl. Phys. Lett.* 93 (2008), 031908.
- [33] M.J. Lai, C.C. Tسان, D. Raabe, On the mechanism of {332} twinning in metastable  $\beta$  titanium alloys, *Acta Mater.* 111 (2016) 173–186.
- [34] C. Zambaldi, S. Zaeferrer, S.I. Wright, Characterization of order domains in-TiAl by orientation microscopy based on electron backscatter diffraction, *J. Appl. Crystallogr.* 42 (2009) 1092–1101.
- [35] X.H. Min, K. Tsuzaki, S. Emura, T. Sawaguchi, S. li, K. Tsuchiya, Tsuchiya, {332}  $\langle 113 \rangle$  Twinning system selection in a  $\beta$ -type Ti–15Mo–5Zr polycrystalline alloy, *Mater. Sci. Eng. A* 579 (2013) 164–169.
- [36] D. Guan, W.M. Rainforth, L. Ma, B. Wynne, J. Gao, Twin recrystallization mechanisms and exceptional contribution to texture evolution during annealing in a magnesium alloy, *Acta Mater.* 126 (2017) 132–144.
- [37] S. Hanada, O. Izumi, Transmission electron microscopic observations of mechanical twinning in metastable beta titanium alloys, *Metall. Trans. A* 17 (1986) 1409–1420.
- [38] T. Furuhashi, K. Kishimoto, T. Maki, Transmission electron microscopy of {332}  $\langle 113 \rangle$  deformation twin in Ti–15V–3Cr–3Sn–3Al alloy, *Mater. Trans.* 35 (1994) 843–850.
- [39] G. Carter, H.M. Flower, G.M. Pennock, D.R.F. West, The deformation characteristics of metastable  $\beta$  -phase in a Ti–15 wt % Mo alloy, *J. Mater. Sci.* 12 (1977) 2149–2153.
- [40] M.A. Meyers, O. Vöhringer, V.A. Lubarda, The onset of twinning in metals: a constitutive description, *Acta Mater.* 49 (2001) 4025–4039.
- [41] K.M. Rahman, V.A. Vorontsov, D. Dye, The effect of grain size on the twin initiation stress in a TWIP steel, *Acta Mater.* 89 (2015) 247–257.
- [42] I. Gutierrez-Urrutia, S. Zaeferrer, D. Raabe, The effect of grain size and grain orientation on deformation twinning in a Fe–22 wt.% Mn–0.6 wt.% C TWIP steel, *Mater. Sci. Eng. A* 527 (2010) 3552–3560.
- [43] E. Ma, T. Zhu, Towards strength–ductility synergy through the design of heterogeneous nanostructures in metals, *Mater. Today* 20 (2017) 323–331.
- [44] Y. Wang, M. Chen, F. Zhou, E. Ma, High tensile ductility in a nanostructured metal, *Nature* 419 (2002) 912.
- [45] H. Zhan, G. Wang, D. Kent, M. Dargusch, The dynamic response of a metastable  $\beta$  Ti–Nb alloy to high strain rates at room and elevated temperatures, *Acta Mater.* 105 (2016) 104–113.
- [46] O. Bouaziz, S. Allain, C. Scott, Effect of grain and twin boundaries on the hardening mechanisms of twinning-induced plasticity steels, *Scripta Mater.* 58 (2008) 484–487.
- [47] Y.F. Shen, Y.D. Wang, X.P. Liu, X. Sun, R. Lin Peng, S.Y. Zhang, L. Zuo, P.K. Liaw, Deformation mechanisms of a 20Mn TWIP steel investigated by in situ neutron diffraction and TEM, *Acta Mater.* 61 (2013) 6093–6106.
- [48] Y.Q. Ning, B.C. Xie, H.Q. Liang, H. Li, X.M. Yang, H.Z. Guo, Dynamic softening behavior of TC18 titanium alloy during hot deformation, *Mater. Des.* 71 (2015) 68–77.
- [49] S. Hanada, M. Ozeki, O. Izumi, Deformation characteristics in  $\beta$  phase Ti–Nb alloys, *Metall. Trans. A* 16 (1985) 789–795.
- [50] M. Besse, P. Castany, T. Gloriant, Mechanisms of deformation in gum metal TNTZ-O and TNTZ titanium alloys: a comparative study on the oxygen influence, *Acta Mater.* 59 (2011) 5982–5988.
- [51] T. Grosdidier, C. Roubaud, M.J. Philippe, Y. Combres, The deformation mechanisms in the  $\beta$ -metastable  $\beta$ -ceZ titanium alloy, *Scripta Mater.* 36 (1997) 21–28.
- [52] M. Ahmed, D. Wexler, G. Casillas, O.M. Ivasishin, E.V. Pereloma, The influence of  $\beta$  phase stability on deformation mode and compressive mechanical properties of Ti–10V–3Fe–3Al alloy, *Acta Mater.* 84 (2015) 124–135.
- [53] P. Yang, Q. Xie, L. Meng, H. Ding, Z. Tang, Dependence of deformation twinning on grain orientation in a high manganese steel, *Scripta Mater.* 55 (2006) 629–631.
- [54] L. Meng, P. Yang, Q. Xie, H. Ding, Z. Tang, Dependence of deformation twinning on grain orientation in compressed high manganese steels, *Scripta Mater.* 56 (2007) 931–934.